Numerical Analysis of Hypersonic Flow Coupled with Radiation around Blunt-Nosed Models

Sanket Razdan

A Thesis Submitted to

Indian Institute of Technology Hyderabad

In Partial Fulfillment of the Requirements for

The Degree of Master of Technology

भारतीय प्रौद्योगिकी संस्थान हैदराबाद
Indian Institute of Technology Hyderabad

Department of Mechanical and Aerospace Engineering

17 June 2019

Declaration

I declare that this written submission represents my ideas in my own words, and where ideas or words of others have been included, I have adequately cited and referenced the original sources. I also declare that I have adhered to all principles of academic honesty and integrity and have not misrepresented or fabricated or falsified any idea/data/fact/source in my submission. I understand that any violation of the above will be a cause for disciplinary action by the Institute and can also evoke penal action from the sources that have thus not been properly cited, or from whom proper permission has not been taken when needed.
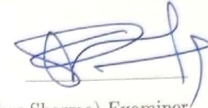
(Signature)

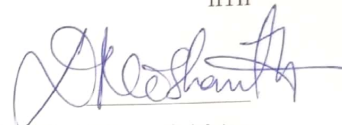(Sanket Razdan)

MEI7MTECH11022

(Roll No.)

Approval Sheet

This Thesis entitled Numerical Analysis of Hypersonic Flow Coupled with Radiaion around Blunt-Nosed Models by Sanket Razdan is approved for the degree of Master of Technology from IIT Hyderabad

(Dr. Chandra Shekhar Sharma) Examiner
Dept. of Chem Eng
IITH

(Dr. Saravanan Balusamy) Examiner
Dept. of MAE
IITH

(Dr. Nishanth Dongari) Adviser
Dept. of MAE
IITH

13/06/2019

Acknowledgements

I am grateful to my instructor Dr. Nishanth Dongari to allow me the freedom to work and at the same time to keep an eye to see that I do not get drifted from the main objective. His mentorship was paramount in providing a well rounded experience consistent my long-term career goals. His honesty and humility, has always motivated us to work harder and has kept us grounded. I am not sure many graduate students are given the opportunity to develop their own individuality and self-sufficiency by being allowed to work with such independence. And simultaneously, he has been the source of motivation for all our friends. Thus, the work environment, I have got to work has been vibrant and energetic.

I would like to thank my group involving Harshal Gijare, Apurva Bhagat and Mandar Ruikar for their valuable suggestions at various points of the thesis and for maintaining an atmosphere of co-operation and friendship. Thus, have made the thesis a joyful experience and journey.

I would like to thank Mechanical and Aerospace Department of IITH and the entire IIT Hyderabad system for providing us an excellent computational facility to work upon.

My highest gratitude goes to Dr.V.K.Saraswat, who came at the point in my academic career that has boosted my interest for working in the area of high-speed flow and radiation.

At last I would like thank my parents and family for their support, patience and faith in me and allowing me to be as ambitious as I wanted. It was under their watchful eye that I gained so much drive and an ability to tackle challenges head on.

Abstract

In the present work, numerical simulations are carried out in a non-continuum hypersonic regime to analyze the flow properties in the shock layer of a blunt body. Radiative transfer equation is added to the existing Navier-Stokes based solver. The solver is developed within OpenFOAM framework and accommodates features to model air chemistry, multispecies transport, thermodynamic properties of high-temperature air, and non-equilibrium boundary conditions.

Simulations involving chemical reactions for high-temperature gases are carried out for Earth and Martian atmosphere. At such temperatures gases tend to dissociate and ionize. Hence, causing lowering of temperature because of endothermic reactions and due to this it also becomes important to solve the species continuity equation along with Navier-Stokes.

The radiative transport equation is solved using spherical harmonics (P1) and finite volume discrete ordinate method (fvDOM) approximations. The aerothermodynamics of high-temperature non-equilibrium flow-field over blunt-nosed models for non-reacting gases have been analyzed using our solver and results are validated with DSMC data. Good agreement has been observed with DSMC data and significant improvement is seen when compared to the conventional high-speed compressible flow solver. The results have shown that a considerable amount of heat escapes from the shock-layer region, hence resulting in radiative cooling. It is observed that, if no radiative heat transfer is considered in the solver, it overpredicts the temperature and shock-layer thickness. Therefore incorporation of radiation along with all the non-equilibrium effects in the rarefied hypersonic regime is imperative.

Contents

List of Figures

List of Tables

Chapter 1

Introduction

1.1 Literature Review

For the efficient design of the modern spacecraft precise understanding of hypersonic flows is very important. When objects are forced to flow at hypersonic speeds, complex shock waves are formed. The shock waves create large discontinuities in terms of pressure, temperature, velocity, and density. The strength of the shock wave increases with increase in Mach number. The high temperature for a typical hypersonic flow causes dissociation and even ionization of the medium. The assumption of calorically perfect gas does not hold here. Therefore, a high-temperature model for the calculation of specific heat capacity, enthalpy and entropy have to be used here. Also, the radiative heat transfer becomes very important when the flow goes beyond Mach 10 because the temperature becomes very high and radiation becomes a dominant mode of heat transfer. Therefore considering all the non-equilibrium effects for such a flow past a blunt body presents a lot of difficulties for accurate solutions in the stagnation region.

The degree of rarefaction is determined by non-dimensional parameter Kn, which is the ratio of the mean free path λ to the characteristic length L. When a hypersonic vehicle enters a planetary atmosphere it travels through the full range of Knudsen numbers from free molecular regime to continuum regime because with altitude the atmospheric density changes. In the free molecular regime since the mean free path is high, the flow encounters a collision-free environment, as it descends further it comes into slip flow regime where the partial collisions between the molecules leads to the formation of shock waves and as the altitude reduces further it comes to continuum regime where temperature and wall heat flux increases sharply. The rarefied slip flow regime mostly operates

in the region of $0.001 < Kn < 0.1$. Hence, Integration of Navier Stokes equation with thermal non-equilibrium effects are very important to accurately predict the shock-flow [1][2]. One of the ways to validate the solver is by comparing the temperature profiles along the stagnation streamline. Another approach is to measure the shock standoff distance that depends on the bluntness of geometry, the degree of rarefaction and radiative heat transfer.

Figure 1.1: Knudsen number based flow regimes.

For the correct prediction of temperature and aerodynamic heating, involving chemically reacting environment is very important. Chemical reaction rates and the coupling between thermochemical phenomena holds some of the largest uncertainties in the modeling of reacting hypersonic flow. Hence, a good knowledge of chemical modeling is also required here.In some models like Gupta et al. [3] both forward and backward reaction rates are there for Earth's atmosphere and in some cases like Park [4][5][6] only forward reaction rates are present for Earth and Martian atmosphere and the calculation for backward reaction rates can be done using equilibrium constant. Flowfield, shock shapes and vehicle surface properties gets affected by the method of computation of backward reaction rates chosen.

For air the threshold temperature, where, the fluid element radiates a substantial amount of energy in a flowfield is about 10000 K. In such case the change in energy occurs because of radiation emitted from the fluid element and also by the absorption of radiation emitted by other fluid elements. Hence, the flowfield becomes nonadiabatic in this case and the total surface heat transfer becomes $q = q_c + q_R$ where q_c includes both conduction and diffusion effects and q_R is the heat transfer by radiation. There can be three different kinds of radiating medium. First is the transparent gas that emits but does not absorb radiation. In this case, all the radiation emitted escapes to the surroundings. The second one is the self absorbing gas. Partial emitted radiation escapes the surroundings and the remaining of it is self absorbed by the medium itself. The third one is the self absorbing scattering medium. For this case, in scattering and out scattering are also considered. The former one increases the value of intensity along a particular direction and the latter decreases it because of intensity scattering to any random direction. In this research work, the second assumption is considered for all simulations.

2
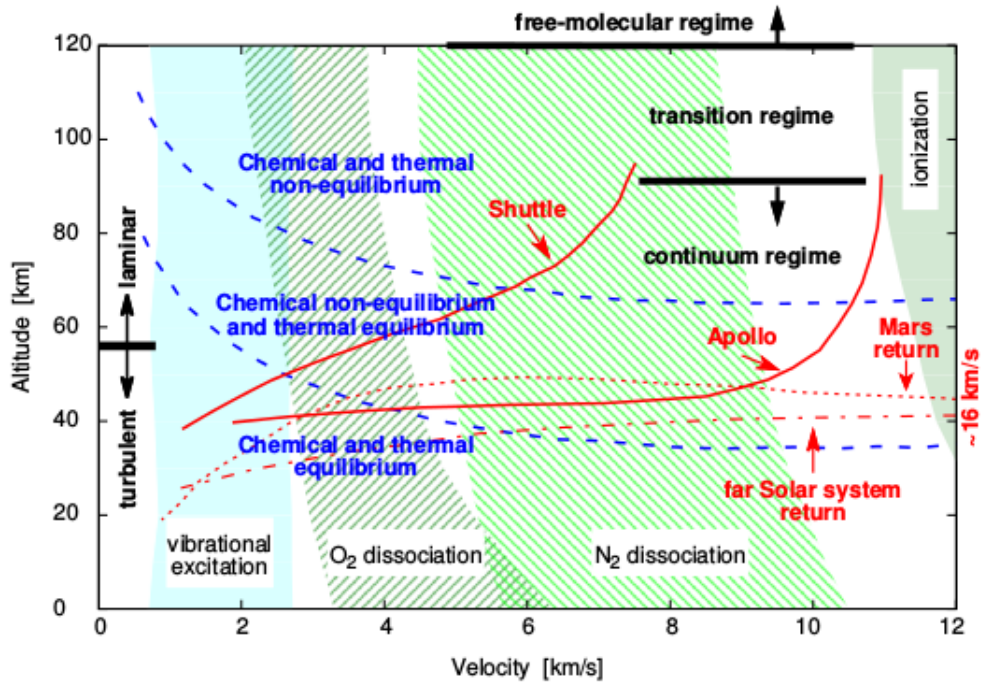
Figure 1.2: Different flow conditions for a reentry hypersonic flight based on velocity and altitude.

Many studies have been performed to study the effect of radiation from the shock layer as well. Radiative heat transfer has been studied for Stardust capsule for non-equilibrium earth reentry conditions [7][8][9]. Liu et al. [7] have solved the Navier Stokes using NASAs CFD code data parallel line relaxation (DPLR) and radiative transfer equation using non-equilibrium radiative transport and spectra program (NEQAIR). Similar studies have been performed for entry into the atmosphere of Titan and Mars. Wright et al. [10] solved for Titan's reentry conditions using DPLR coupled with one- dimensional tangent slab method and view factor-based approach. Bansal et al. [11] solved for crew exploration vehicle (CEV) for the Martian atmosphere using OpenFOAM. They used existing radiation models available in OpenFOAM mainly P1, to solve for radiative transfer equation. Their solver is validated with NASA's standard DPLR code. The stagnation-point radiative heat transfer exceeds the convective heat transfer at high velocities. Thinning of the shock layer is also observed due to coupled radiation.

OpenFOAM (open-source field operation and manipulation) [12] has the capability to solve the compressible flow equations on unstructured 3-D meshes. Mesh can be created externally and imported into OpenFOAM. OpenFOAM provides with a comprehensive number of C++ libraries, which can be manipulated to add new features into the existing solvers. New flow solvers can be developed by modeling various mathematical operators to change or write new flow equations .

OpenFOAM is incorporated with many flow solvers that have been validated by a large number of users for a large number of problems related to heat transfer, combustion and fluid mechanics. The rarefiedHypersonicFoam solver is developed in the current work combining a number of features of two existing solvers rhoCentralFoam and reactingFoam. The former is a density-based compressible N-S flow solver based on central-upwind schemes of Kurganov and Tadmor [13][14].

The solver is valid for low hypersonic flights ($Ma < 10$) and temperature up to 2,000 K. Hence, it is not sufficient to model gas properties at higher temperatures ($T >> 2000K$). The latter is a pressure-based solver for chemically reacting combustion problems. The reactingFoam provides a number of features, such as species transport, chemical kinetics and thermodynamic properties based on chemkin format and data. OpenFOAM's thermodynamic data is valid till 6000 K and therefore are not sufficient to model gas properties at higher temperatures. Hence, the OpenFOAM's thermodynamic library was updated with data from Gordan and Mcbride [15], which provides polynomial fits for thermodynamic properties of a large number of species, and is valid up to 20,000 K. A kinetic theory based model is used to calculate laminar viscosity and thermal conductivity of the flow. Also, a single temperature model is used to solve flow problems. The same practice was first adopted by Bansal et al. for creating a hypersonic solver [11]. The first-order velocity slip and temperature jump boundary conditions are used in our solver to extend its applicability to slip flow regime. The rarefiedHypersonicFoam without coupled radiative transfer has been validated by Gijare et al. for a number of test cases [16][17].

The major objective is to develop and validate a solver within OpenFOAM framework which is capable of solving problems related to high-temperature gas flows ($Ma > 10$) and altitude ranging from 40-70 km. The major novelty of this study is to compute the radiative transfer equation coupled with a rarefiedHypersonicFoam using a computationally expensive but much accurate fvDOM to establish better results for a high-temperature flow case in terms of temperature and shock standoff distance.

1.2 Objectives of Present Work

- To implement new thermophysical model valid upto 20000 K in *rarefiedHypersonicFoam* solver

- To validate the solver for single species, high-temperature and non-reacting hypersonic flow against DSMC data using first-order Maxwells velocity slip and the Smoluchowski temperature jump boundary conditions.

- Validate the solver for high-temperature chemically reacting flows.

- Couple radiation with *rarefiedHypersonicFoam* solver.

- Plot the flowfield properties along the stagnation streamline.

- Compare the temperature plots and contours alongwith shock thickness for with and without radiation for reacting and non-reacting flows.

Chapter 2

Numerical Methodology

2.1 Governing Equations

The governing equations that we solve are in Eulerian framework. The equations are derived using the conservation laws of fluid motion. Finite volume discretization is used for the solving the partial differential equations. The mass conservation equation of species is given as [1][14]:

$$\frac{\partial \rho Y_i}{\partial t} + \nabla.[\vec{u}\rho Y_i] - \nabla.[\rho D_i \nabla Y_i] - w_i = 0 \tag{2.1}$$

where the terms sequentially from left represent rate of change of mass of species i per unit volume, mass flux convected across cell faces, mass diffusion due to concentration gradients and mass production rate due to chemical reactions respectively. Y_i is the species mass fraction, D_i is diffusion of species i in gas mixture, ρ is density and $\vec{u}$ is velocity vector. The global mass conservation equation is written as [10]: The global mass conservation equation (continuity equation) is written as [1][14]:

$$\frac{\partial \rho}{\partial t} + \nabla.[\vec{u}\rho] = 0 \tag{2.2}$$

where the terms sequentially from left represent the rate of change of mass density and the flux of mass density across cell faces, ρ is density and $\vec{u}$ is velocity vector. The equation for conservation of momentum is summarized below [1][14]:

$$\frac{\partial (\rho \vec{u})}{\partial t} + \nabla.[\vec{u}(\rho \vec{u})] + \nabla p + \nabla.\sigma = 0 \tag{2.3}$$

6

where the terms sequentially from left represent the rate of change of momentum per unit volume, the flux of momentum across the cell faces, pressure forces acting on the cell walls and viscous forces acting on cell faces respectively. The shear stress tensor σ is given as:

$$\sigma = \mu(\nabla \vec{u} + \nabla(\vec{u})^T - 2/3\nabla.\vec{u}) \tag{2.4}$$

The radiation term is incorporated and then the energy equation is written as [1][2]:

$$\frac{\partial(\rho E)}{\partial t} + \nabla.[\vec{u}(\rho E)] + \nabla.(\sigma.\vec{u}) - \nabla.(k\nabla T) - \nabla[\rho \sum_i h_i D_i \nabla Y_i] + \nabla.q_{rad} = 0 \tag{2.5}$$

where the terms sequentially from left represent the rate of change of total energy per unit volume, the flux of total enthalpy across cell faces, work done by shear forces, conduction of energy due to temperature gradients, diffusion of enthalpy due to concentration gradients and rate of energy loss due to radiation respectively. ρE is total energy of the system, k is thermal conductivity, T is temperature and $E = e + |\vec{u}^2|/2$, where $e = C_v T = (\gamma - 1)RT$ represents the specific internal energy and $\gamma = C_p/C_v$ represents the ratio of specific heats at constant pressure and volume. The value of the temperature is calculated by the total energy, iteratively.

$$T = \frac{1}{C_v(T)}[E(T) - |\vec{u}|^2/2] \tag{2.6}$$

$$C_p = \frac{P}{1/2\rho_\infty u_\infty^2} \tag{2.7}$$

where C_p is the coefficient of pressure, P is the static pressure, ρ_∞ is the freestream density and u_∞ is the freestream velocity.

2.2   Transport Properties

Laminar viscosity is calculated as [18]:

$$\mu_i = 2.6693 \times 10^{-5} \frac{\sqrt{M_i T}}{d_i^2 \Omega_\mu} \tag{2.8}$$

where Ω_μ is the collision integral, M_i and d_i are molecular weight and characteristic molecular diameter, respectively. Values of Ω_μ as a function of $k_1 T/\epsilon$ are tabulated in [18], where k_1 is the Boltzmann constant and ϵ is the characteristic molecular energy of interaction. Values of d and

ϵ/k_1 are associated with Lennard-Jones potential that is tabulated in [1]. Effective viscosity (μ_{eff}) is calculated from laminar and turbulent viscosity. Thermal conductivity is calculated by Euckens relation [19]:

$$k_i = \mu_i(C_p + \frac{5}{4}R) \tag{2.9}$$

where k_i is the thermal conductivity of species i. Mixture values of μ and k are calculated as the weighted average of μ_i and k_i based on the mole fraction of species. Binary diffusion coefficient for species i diffusing in species j is calculated as:

$$D_{ij} = \frac{10.1325(0.001858 \times T^{1.5}\sqrt{\frac{1}{M_i} + \frac{1}{M_j}})}{pd_{ij}^2\Omega_{d,ij}} \tag{2.10}$$

where d_{ij} is approximated as:

$$d_{ij} = \frac{1}{2}(d_i + d_j) \tag{2.11}$$

where values for $\Omega_{d,ij}$ as a function of $k_1 T/\epsilon_{ij}$ are given in [1] and $\epsilon_{ij} = \sqrt{\epsilon_i\epsilon_j}$. Multicomponent diffusion coefficient D_{im}, for diffusion of specie i into mixture m, is calculated as:

$$D_{im} = \frac{1 - X_i}{\sum_j \frac{X_j}{D_{ij}}} \tag{2.12}$$

The simulations are done for laminar cases as the Reynolds number < 2000 because density is very low.

2.3 Boundary Conditions

Since the cases mostly occur in the Kn ranging from 0.001 to 0.1, hence, continous boundary conditions for Temperature and no slip condition for velocity cannot be used here as the full momentum transfer does not happen in slip flow regime. The Maxwell's slip boundary condition is describes as [20]:

$$u_f - u_w = \frac{2 - \sigma_v}{\sigma_v}\lambda\frac{\partial u}{\partial y} + \frac{3\mu}{4\rho T}\frac{\partial T}{\partial x} \tag{2.13}$$

where u_f is the fluid velocity, u_w is the reference wall velocity, x is the axial co-ordinate, y is the normal co-ordinate and σ_v is tangential momentum accommodation coefficient.

Smoluchowski Temperature Jump is defined as [21]:

$$T_f - T_w = \frac{2 - \sigma_T}{\sigma_T}\frac{2\gamma}{\gamma + 1}\frac{\lambda}{Pr}\frac{\partial T}{\partial y} \tag{2.14}$$

and

$$Pr = \frac{\mu C_p}{k} \tag{2.15}$$

where T_f is the temperature of fluid, T_w is the reference wall temperature, Pr is the non-dimensional Prandtl number, σ_T is thermal accommodation coefficient.

2.4 Radiative Modeling

The radiative heat transfer equation is expressed as [2]:

$$\frac{dI_{r,s}}{ds'} = \nabla(I_{r,s}) = k_e I_{b,r} - (k_a + \sigma_{eff})I_{r,s} - \frac{\sigma_{eff}}{4\pi} \int_{4\pi} I_{r,s^*} \phi(s^*,s)d\Omega^* \tag{2.16}$$

where $I_{r,s}$ is the radiation intensity that at the r point that propagates along s direction, s', is the coordinate along that direction, s^* is the scattering direction vector, $I_{b,r}$ is the black body radiation intensity at point r, k_a is the absorption coefficient, k_e is the emission coefficient, σ_{eff} is the scattering coefficient, $\phi_{s^*,s}$ is the scattering phase function and Ω^* is the solid angle.

The radiative heat transfer equation is simplified using spherical harmonics approximation (P1 method) [2]. Using this approximation we obtain a simplified form of the differential equation for the calculation of incident radiation flux G, through which we can calculate $\nabla.q_{rad}$, which is provided as a source term in Eq. 2.5. The P1 equation in OpenFOAM [12] is written as:

$$\nabla.(\tau \nabla G) - k_a \nabla G = -4(k_{SB}k_e T^4 + E_1) \tag{2.17}$$

where $\tau = \frac{1}{3k_a + \sigma_{eff}}$, k_{SB} is Stefan-Boltzmann constant and E_1 is the emission contribution. Marshak's boundary condition is used with the P1 model for coupled radiation case [2]:

$$\tau(\hat{n}.\nabla G_w) = -\frac{\epsilon_w(4\sigma T_w^4 - G_w)}{2(2 - \epsilon_w)} \tag{2.18}$$

where $\hat{n}$ is the unit normal vector to the wall, G_w is the incident radiation flux at the wall, T_w is the calculated wall temperature and ϵ_w is the emissivity. Then the divergence of radiative heat flux is calculated as:

$$\nabla.q_{rad} = k_a G - 4(k_e k_{SB} T^4 + E_1) \tag{2.19}$$

The fvDOM radiation model solves for a discrete number of finite solid angles where the radiative

9

transfer Eq. 2.16 is directly solved for r points and s directions in a participating media [2]. The radiative source term $\nabla.q_{rad}$ in the enthalpy Eq. 2.5 is calculated from the total radiation flux G. The total radiation flux can be obtained by integrating the radiation intensity over all possible directions and across all possible points. A diffusely emitting and reflecting boundary condition is used with the fvDOM model for inlet, outlet, and wall [2].

$$I_{r,s} = \epsilon_w I_{b,r} + \frac{1 - \epsilon_w}{\pi} \int\limits_{\hat{n}.\hat{s}>0} I(r,\hat{s})|\hat{n}.\hat{s}|d\Omega \tag{2.20}$$

2.5   Algorithm for *rarefiedHypersonicFoam*

- The time step starts with the initialization of u, p, T, Y_i, ρ, ρu, E.

- Transport properties variables σ, μ_i, k_i and D_{ij} are updated using Kt Transport model.

- The continuity equation is solved for ρ.

- In the next step species continuity equation for each species i is solved for Y_i. In this step w_i input is required which comes from chemical kinetic model used and then new ρ is calculated as $\frac{p}{RT\sum_i \frac{Y_i}{M_i}}$.

- In the predictor step, inviscid momentum equation is solved explicitally and u is updated.

- Boundary conditions for u is applied and ρu_b is calculated as $u_b \times \rho_b$.

- Then, in the corrector step, diffusion momentum equation is solved implicitly and u is updated.

- In a similar way, inviscid energy equation is solved for E as a predictor step and T is updated from E, u and ρ as $C_p T = \frac{\rho E}{\rho} - |u|^2/2$.

- Boundary conditions for T is applied and E is calculated.

- The diffusion energy equation $+ \nabla.[\rho \sum_i h_i D_i \nabla Y_i] + \nabla.q_{rad}$ is solved as the corrector step and T is updated implicitly.

- In the final step, considering the gas as ideal p is updated as ρRT.

- The current time step ends here.

Chapter 3

Validations

3.1 Blunted Flat Plate
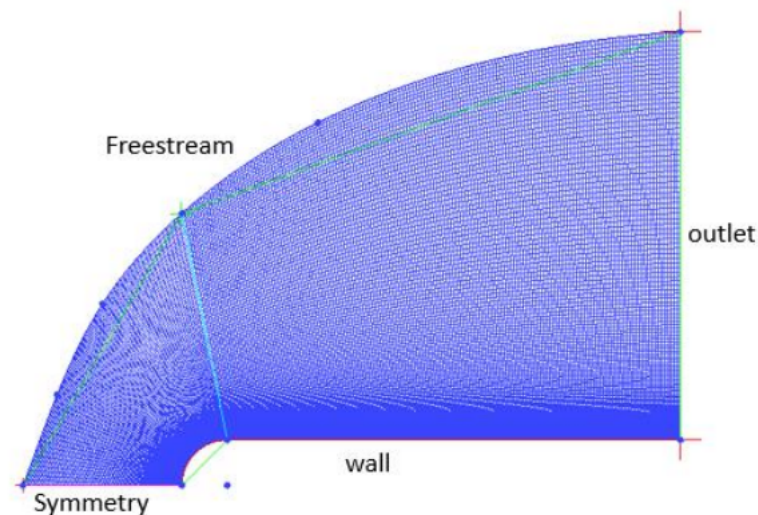
Figure 3.1: Computational domain and grid for cylindrically blunted flat plate case

Simulations have been carried out for flow over cylindrically blunted flat plate with Argon adopted as test gas using rarefiedHypersonicFoam and the geometry is presented in Figure 3.1. The flow conditions are given in Table 3.1. The initial cell size for the finest mesh is taken as $\delta y = 1.9e - 06$ and $\delta x = 5.78e - 04$ to accurately capture the near wall effects. y in the mesh is increased by 10 % while moving away from the wall, and mesh file is imported from ICEMCFD to OpenFOAM using fluentMeshToFoam utility. The simulation is done in an slip flow regime defined by Knudsen number, which is described as $Kn = \lambda/R$ where λ is the mean free path of the medium and

R is the characteristic dimension. Maxwell velocity slip [20] and Smoluchowski temperature jump [21] boundary conditions are used in the solver to extend its applicability to the slip flow regime. Constant absorption, emission model and non- scattering medium is considered for the simulation. The value for absorption and emission coefficient in this case is taken as 0.5 1/m [22][23][24]. Marshaks boundary conditions is used at inlet, outlet and wall with emissivity values of 1, 1 and 0.85 respectively.

Table 3.1: Flow simulation conditions for blunted flat plate.

Test gas	Kn	$R(m)$	Type	Ma_∞	p_∞(Pa)	ρ_∞(kg/m^3)	T_∞(K)
Argon	0.1	0.010	2D	10	5.29	1.142e-04	219.585

The fvDOM model coefficients are defined as $nPhi = 4$ and $nTheta = 0$, the convergence criteria for radiation iteration is 10^-3 and $maxIter = 4$ for the maximum number of iterations. $nPhi$ indicates that the direction of ray is in x-y plane and it denotes the azimuthal angle is $\pi/2$. Only $nPhi$ is considered in this case as it is a 2D geometry and the direction of ray is on x-y plane. 12 rays are allocated from I_0 to I_{11} with an average orientation omega of 1.0472 rad [25]. For fvDOM model additional boundary condition for I is also defined.
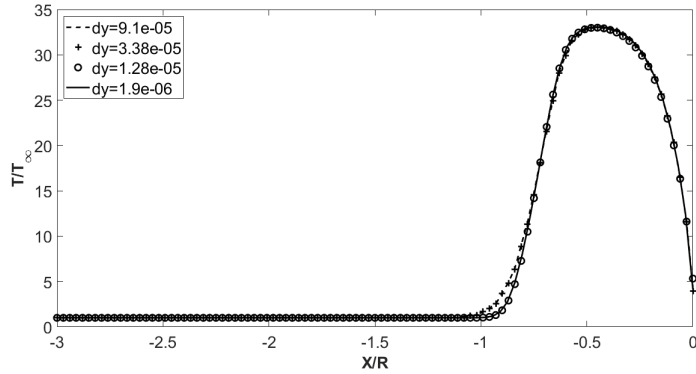
Figure 3.2: Grid Independence study for blunted flat plate case for four different meshes, where normalized temperature variation is presented along the stagnation streamline.

In Figure 3.2, the grid independence study is carried out for four different meshes varying from coarse to fine near the wall. A slight difference in predicting the shock-layer thickness between the coarse and finemeshes is observed. The error between the results of the two finest meshes is found within 1 %. In Figure 3.3a, the distribution of normalized temperature along the stagnation streamline is compared with those of the DSMC generated by OpenFOAM [12] and the in-house N-S solver (UNS) of Massimi et al. [26]. Courant Friedrichs Lewy (CFL) is set to 0.01 for the initial phase of the flow development and is gradually increased to 0.1 and 0.5 as the flow is developed

in the fore-body region. It can be seen that the *rarefiedHypersonicFoam* solver performs better than the UNS code and is in good agreement with the DSMC results. However, the shock thickness obtained by the solver is slightly lower than the DSMC result as the Knudsen number is 0.1 and continuum breakdown happens within the shock layer. Results have shown good agreement with the DSMC data in the boundary layer region ($-0.5 < X/R < 0$). The shock layer comes out to be more diffused in rarefiedHypersonicFoam compared with UNS due to the incorporation of non-equilibrium effects. A deviation of about 46.66 % comes out for shock thickness of UNS code compared to DSMC while for rarefiedHypersonicFoam it is 33.33 %.
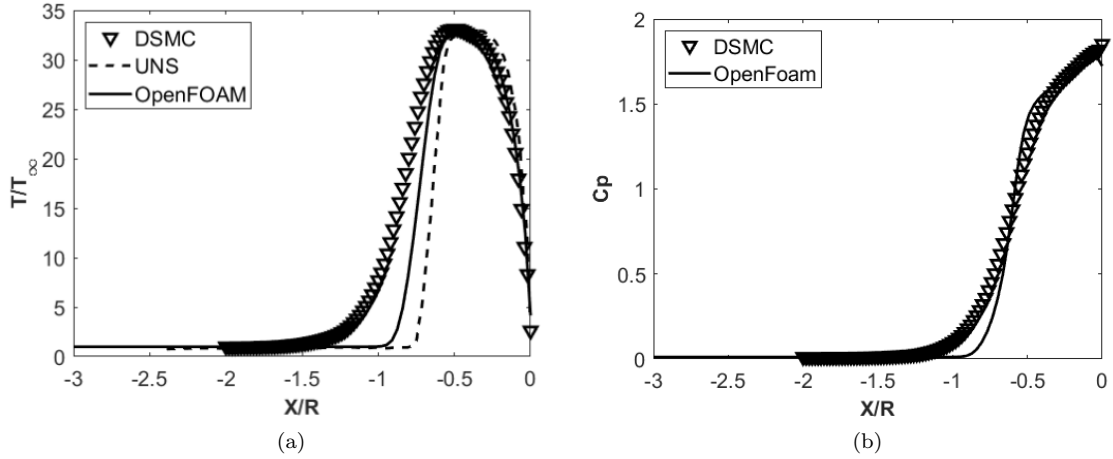

Figure 3.3: Distribution of (a) normalised temperature and (b) coefficient of pressure along the stagnation streamline.

Similarly, the coefficient of pressure (C_p) shows good agreement with DSMC data. In Figure 3.3b it can be seen that both the shock layer and boundary layer merge into one another, which makes it very difficult to distinguish between the two. Thats why its very complicated to analytically calculate the flow properties in a hypersonic flow and hence, we sought to non-equilibrium based numerical methods.

In Figure 3.4, the temperature profile along the stagnation streamlines is plotted for coupled radiation solver using P1 and fvDOM approximations. The shock-layer loses heat to its surroundings by radiation and hence, a difference of around 750 K between the peak values is seen for with and without radiation cases The loss of heat also reduces the shock-layer thickness. Good agreement is seen between P1 and fvDOM model in terms of prediction of peak values and hypersonic boundary layer region. The shock layer region is an optically thin region in this case. Almost 20 % reduction for P1 and 30 % reduction for the fvDOM model in terms of shock thickness is seen. An increase in the inlet temperature by 127 % along the stagnation streamline is observed for fvDOM because
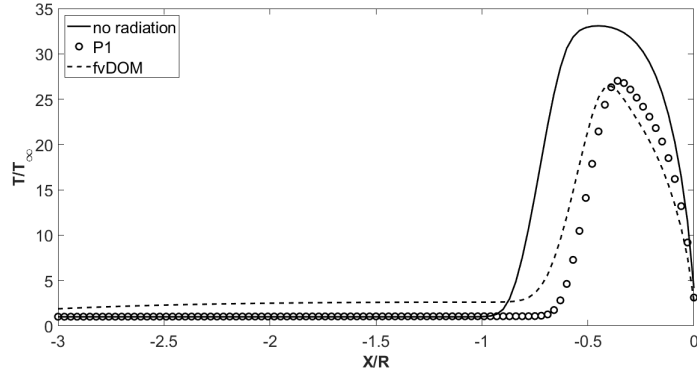
13

Figure 3.4: Comparison of normalized temperature along the stagnation streamline for with and without radiation.

of the assumption that the absorption and emission coefficient of the participating media remains constant but in reality, it depends upon wavelength, temperature, and composition of the medium. Hence, both fvDOM and P1 method almost provide similar trends for the temperature profile but for an optically thin medium better prediction will be given by fvDOM compared to P1, though it is computationally expensive.
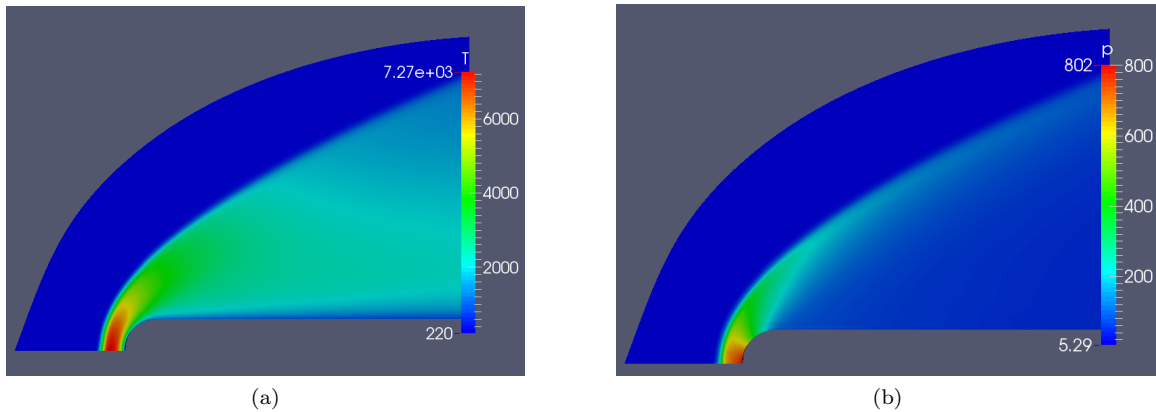
Figure 3.5: Contours of (a) Temperature and (b) Pressure for cylindrically blunted flat plate.

In Figure 3.5a and 3.5b contours for temperature and pressure is shown. The bow shock is clearly visible in both the contours. The stagnation region is very important because the temperature and pressure in that region increases immensely.In hypersonic flows blunt bodies are preferred because detached shocks are formed for such cases as if there is a sharp corner, oblique attached shock will be formed and the temperature at the stagnation point will be very large. In Figure 3.6a and 3.6b it can be seen how the temperature and shock thickness drops down when the solver is coupled with radiation, although the shock pattern remains the same.
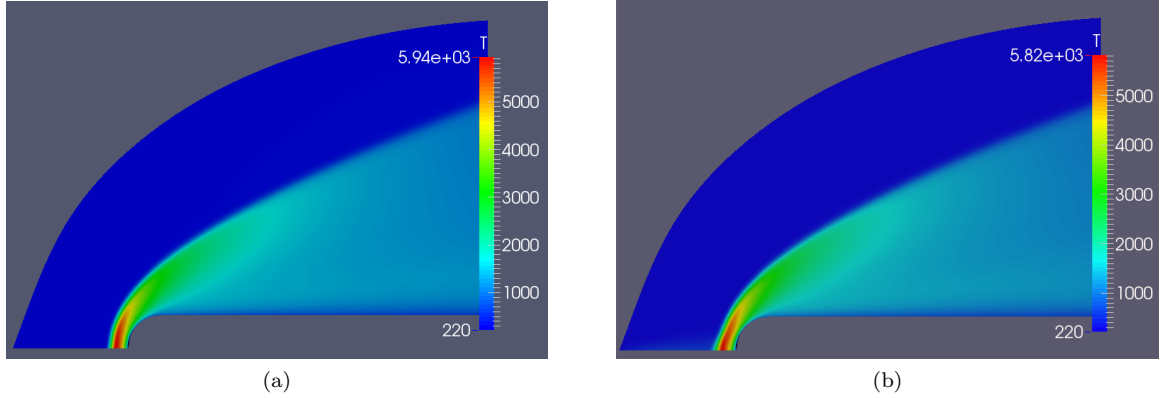
Figure 3.6: Contours of Temperature for (a) P1 and (b) fvDOM model.

3.2 Blunted Wedge Geometry
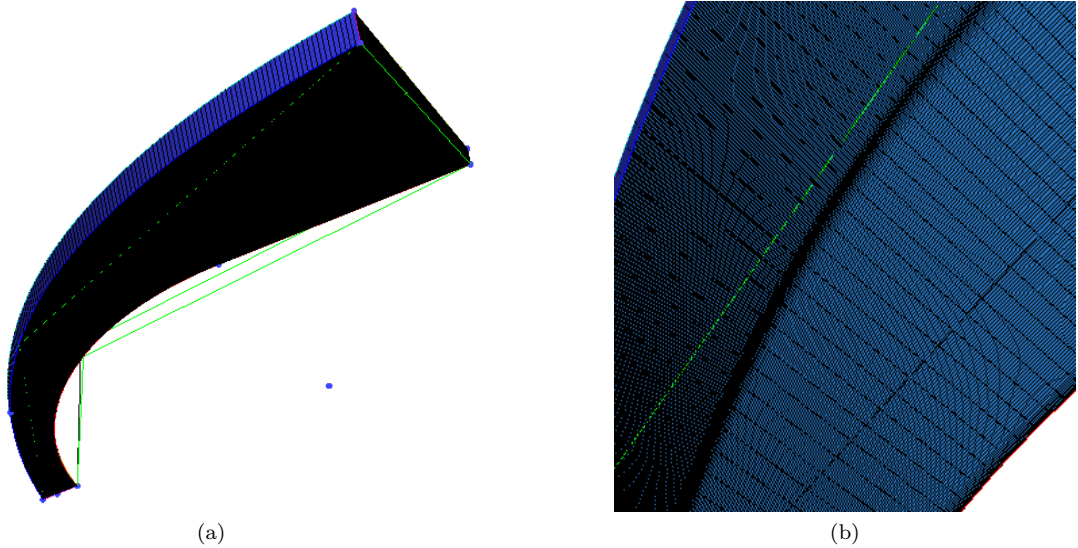
Figure 3.7: (a) Grid generation and (b) zoomed in view of the mesh for blunted wedge geometry.

The second case is done for blunted wedge geometry [27] using $rarefiedHypersonicFoam$ with dry air as the test gas presented in Figure 3.7a to validate its capability to predict hypersonic chemical dissociation of flow fields. The flow conditions are given in Table 3.2 [27]. CFL no is used in this case to calculate the time step. At the wall velocity slip and temperature jump boundary conditions are used, inlet condition is hypersonic, outlet condition is zero gradient or supersonic and symmetry is assumed along the stagnation steamline. Also, in the present calculations a non-catalytic wall is assumed. The geometry type is considered as wedge in this case, so that more realistic results can be predicted compared to 2D.

Table 3.2: Flow simulation conditions for blunted wedge geometry.

Test gas	Kn	$R(m)$	Type	Ma_∞	p_∞(Pa)	ρ_∞(kg/m^3)	T_∞(K)	T_w(K)
Dry air	0.00205	0.0066	wedge	18	432.2	5.97e-05	252.0	555.5

Table 3.3: Arrhenius forward reaction rates for a five-species air model.

Forward Reaction	$A(\frac{cm^3}{mols})$	β	$E_a(K)$
$O_2 + M \rightarrow 2O + M$	3.61×10^{18}	-1.0	-5.94×10^4
$N_2 + M \rightarrow 2N + M$	1.92×10^{17}	-0.5	-1.131×10^5
$N_2 + N \rightarrow 2N + N$	4.15×10^{22}	-1.5	-1.131×10^5
$NO + M \rightarrow N + O + M$	3.97×10^{20}	-1.5	-7.56×10^4
$NO + O \rightarrow O_2 + N$	3.18×10^9	1.0	-1.97×10^4
$N_2 + O \rightarrow NO + N$	6.75×10^{13}	0	-3.75×10^4

The composition of dry air is taken as 79 % of N_2 and 21 % of O_2. When the temperature in the shock layer region reaches above 2500 K, then O_2 dissociates to form O and when the temperature further goes above 4000 K then $N2$ starts to dissociate to form N. Exchange reaction to form NO species also takes place in this temperature range.So, for such cases air chemistry is modeled using 5 species i.e. N_2, O_2, N, O, NO having 6 forward reactions and 6 backward reactions, the data for the same has been taken from Gupta *et al.* [3]. In this case ionization reaction have been neglected. Using the Arrhenius reaction rates parameters provided in Table 3.3 and 3.4, the reaction rates are calculated as:

$$r = AT^\beta exp(\frac{E_a}{T}) \tag{3.1}$$

where A and β are Arrhenius rate parameters, while E_a is the ratio of activation energy E_{ae} (cal/mol) to the universal gas constant. The state of the gas in this case is governed by single equilibrium temperature as all the species are assumed to be in thermal equilibrium.
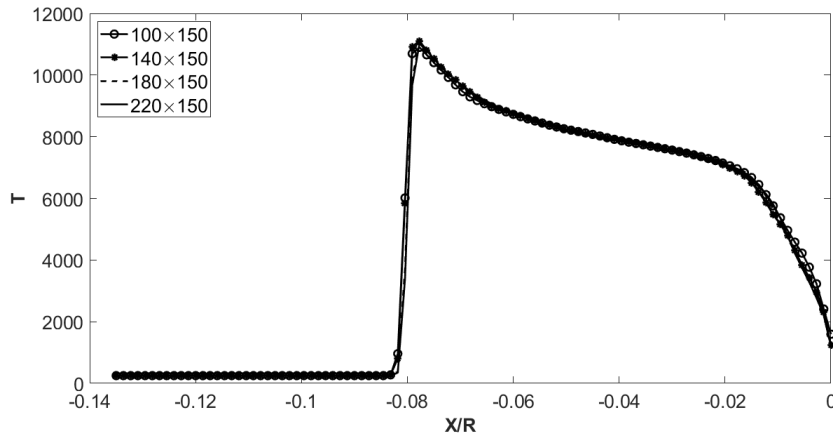

Figure 3.8: Grid independence study for blunted wedge geometry

Table 3.4: Arrhenius backward reaction rates for a five-species air model.

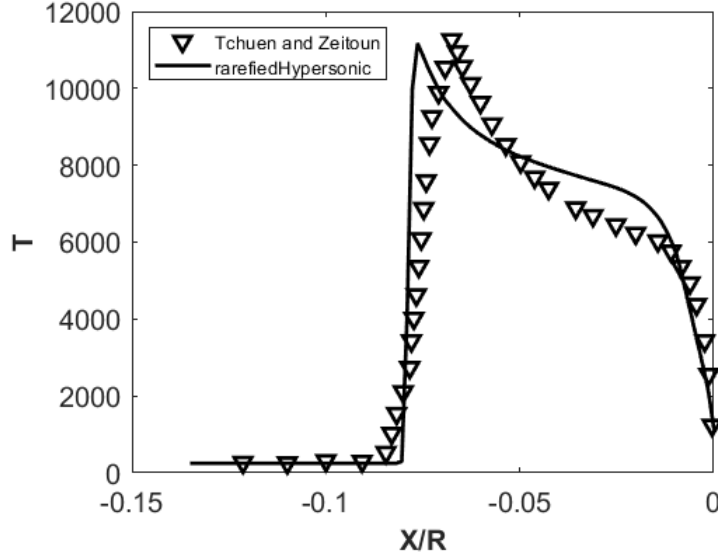| Backward Reaction	$A(\frac{cm^3}{mol-s} \, or \, \frac{cm^6}{mol^2-s})$	β	$E_a(K)$
$2O + M \rightarrow O_2 + M$	3.01×10^{15}	-0.5	0
$2N + M \rightarrow N_2 + M$	1.09×10^{16}	-0.5	0
$2N + N \rightarrow N_2 + N$	2.32×10^{21}	-1.5	0
$N + O + M \rightarrow NO + M$	1.01×10^{20}	-1.5	0
$O_2 + N \rightarrow NO + O$	9.63×10^{11}	0.5	-3.6×10^3
$NO + N \rightarrow N_2 + O$	1.5×10^{13}	0	0

Figure 3.9: Comparison of temperature profiles along the stagnation streamline between $rarefiedHypersonicFOAM$ results and those of Tchuen & Zeitoun

In Figure 3.8, grid independence study with temperature profile is done for this case. The simulation is first done on a coarse mesh and to get better results mesh is made finer near the wall and across the shock region. 100 cells in the normal direction and 150 along the direction body are used intially. Then 10 cells in the boundary layer and 20 cells across the shock region are added with each level of fineness. The error between the two finest meshes is within 1 %. In Figure 3.9 the temperature profile is plotted along the stagnation streamline. The plot is compared with the results from Tchuen and Zeitoun [27]. It can be clearly seen that $rarefiedHypersonicFOAM$ results matches with Tchuen and Zeitoun. A good match is seen before the shock and near to the wall region. Slight shifting of the curve towards the left is observed. In the shock-stand off distance a deviation of about 10.44 % is seen. Also, the peak temperature predicted by $rarefiedHypersonicFOAM$ is less than that of Tchuen and Zeitoun. About 2.25 % deviation is seen in the prediction of peak temperature. The reason behind this is the inclusion of two temperature model by Tchuen and Zeitoun. The effects from both translational and vibrational tenperature have been considered by

17

Tchuen and Zeitoun in this case, on the other hand single temperature model assumption is used to simulate this case using $rarefiedHypersonicFOAM$.

Behind the shock translational temperature reaches to its peak value quickly whereas vibrational temperature takes more time to reach its equilibrium value. Hence, a model only driven by translational temperature will tend to overpredict the dissociations happening in the shock-layer region. That is why an under predicted temperature peak value is seen in $rarefiedHypersonicFOAM's$ case. In addition to this a smooth nature of the temperature profile is seen in the boundary layer region because the chemical reactions are endothermic and they draw heat from the shock-layer which results in lowering of temperature and shock stand-off distance.

In Figure 3.10a and 3.10b the mass fraction profiles for N_2 and O_2 are plotted. Tchuen and Zeitoun have used Park's model for forward reaction rates and backward reaction rates are computed using equilibrium constant K_{eq}. The equilibrium constant is calculated analytically with minimization of Gibb's free energy of each species under thermodynamic assumptions [19]. It is also calculated using Gupta's [3] least square fit of experimental data involving six parameters.

$$K_{eq} = \frac{K_f}{K_b} \tag{3.2}$$

$$K_{eq} = exp(a_1 z^5 + a_2 z^4 + a_3 z^3 + a_4 z^2 + a_5 z + a_6) \tag{3.3}$$
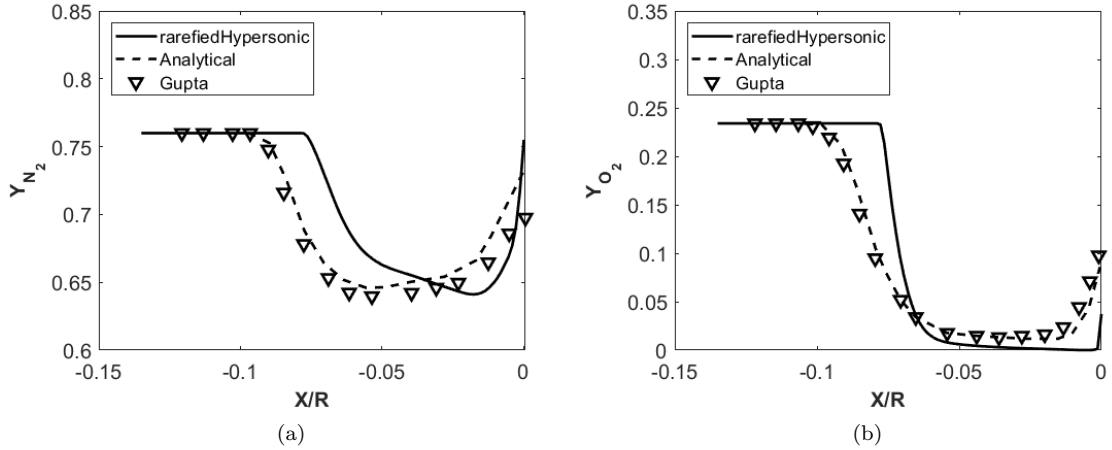
where $z = \frac{10000}{T}$

Figure 3.10: Comparison of mass fraction profiles along the stagnation streamline for (a)N_2 and (b)O_2.

Behind the shock, the mass fraction for N_2 and O_2 drops significantly because the tempera-

ture sharply increases which leads to dissociation of N_2 and O_2. Since the shock thickness for *rarefiedypersonicFoam* is less than Tchuen and Zeitoun, hence the dissociation starts early for this case. The curve nature for both N_2 and O_2 profiles are similar to analytic and Gupta's approach. A good match is seen near the stagnation point for the mass fraction profile of N_2. Near the stagnation point the mass fraction for N_2 again increases. This is because exchnage reaction between N_2 and O forms NO, which further starts dissociating and simultaneous exchange reactions leads to the formation of N_2. Also, because of the dissociation of NO, its mass fraction decreases near stagnation point. In Figure 3.11a, 3.11b, 3.12a and 3.12b, the contours for temperature, pressure and mass fractions of N_2 and O_2 are presented.
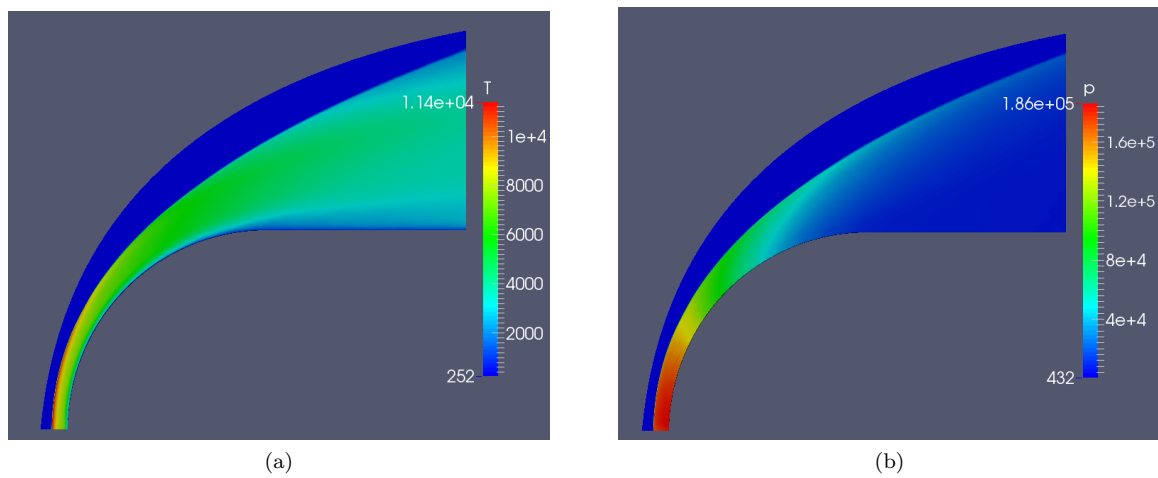

(a)   (b)

Figure 3.11: Contours of (a) Temperature and (b) Pressure for blunt wedge geometry.
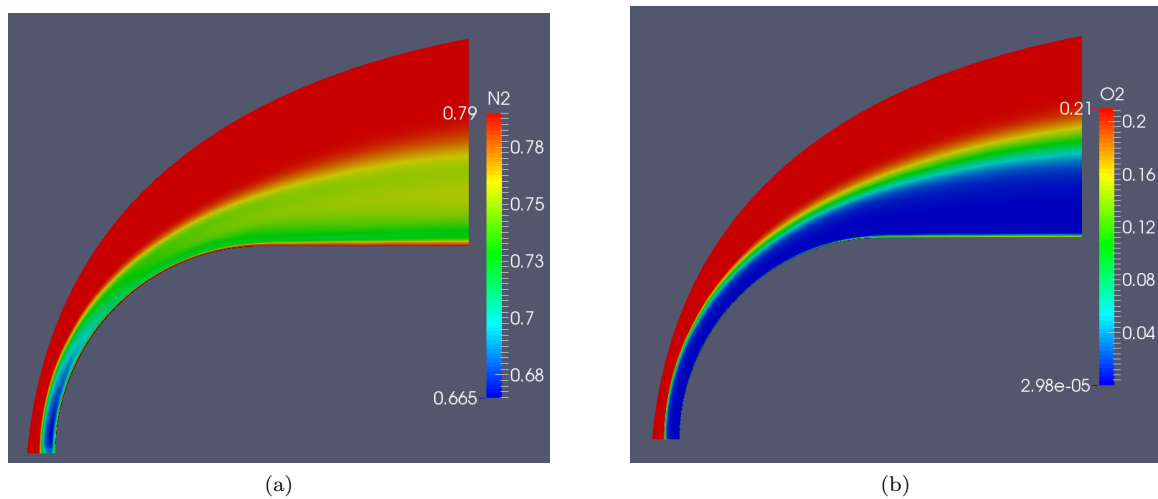

(a)   (b)

Figure 3.12: Contours of (a) N_2 and (b) O_2 for blunt wedge geometry.

Chapter 4

Analysis
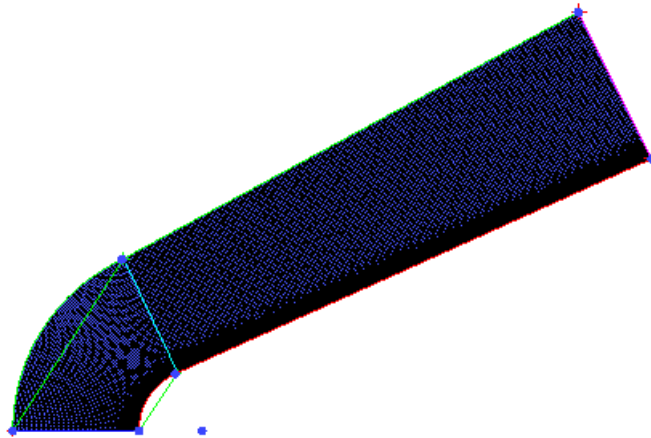
4.1   Blunted Cone

Figure 4.1: Computational domain for blunted cone case

Simulations have been carried out at 5 km/s past a blunted cone with non-reacting N_2 as the test gas. The case is composed of a 6.35 mm radius nose followed by a flat plate forming a 25 degrees angle with the free-stream flow direction and whose streamwise extension is 5 cm [28]. The flow conditions are given in Table 4.1. In Figure 4.1, the 2D axisymmetric grid for the same is shown. The initial cell size for the finest mesh is taken as $\delta y = 1e - 06$ and $\delta x = 1.5e - 04$ to accurately capture the near wall effects. The mesh consists of 100×250 cells. The flow conditions for the same is given in Table 4.1.

Since the case falls under slip flow regime, hence velocity slip and temperature jump boundary

Table 4.1: Flow simulation conditions for blunted cone case.

Test gas	Kn	$R(m)$	Type	Ma_∞	p_∞(Pa)	ρ_∞(kg/m^3)	T_∞(K)
N_2	0.002	0.00635	2D	20	21.9139	5.113e-04	144.4

conditions are used here. The case is first run without radiation, then P1 model is used with Marshak's boundary conditions at the inlet, outlet and wall. The radiative equation of G that we obtain after using spherical harmonics simplification is solved once for every 5 iterations. Constant absorption, emission model and non- scattering medium is considered for the simulation. The value for absorption and emission coefficient in this case is taken as 0.5 1/m. After P1, the case is also solved using fvDOM. The fvDOM model coefficients are defined as $nPhi = 4$ and $nTheta = 0$, the convergence criteria for radiation iteration is 10^-3 and $maxIter = 4$ for the maximum number of iterations. $nPhi$ indicates that the direction of ray is in x-y plane and it denotes the azimuthal angle is $\pi/2$. Only $nPhi$ is considered in this case as it is a 2D geometry and the direction of ray is on x-y plane. 12 rays are allocated from I_0 to I_{11} with an average orientation omega of 1.0472 rad [25]. For fvDOM model a diffusely emitting and radiating surface boundary condition is used at inlet, outlet and wall.
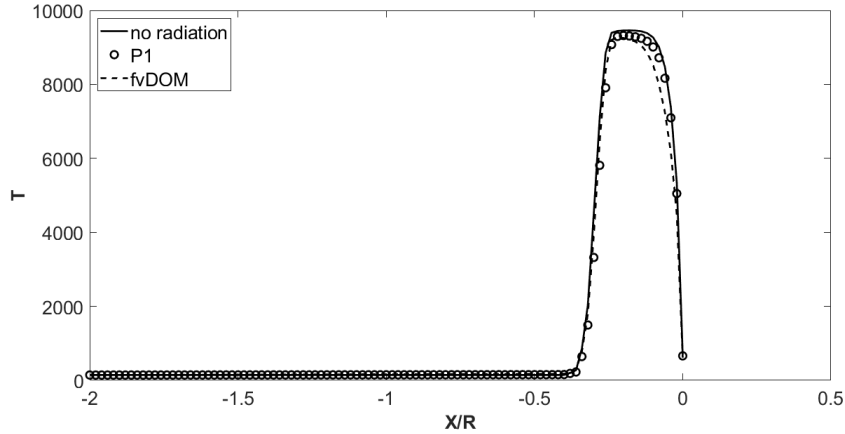

Figure 4.2: Comparison of temperature profile along the stagnation streamline for no radiation, P1 and fvDOM

In Figure 4.2 the temperature profiles along the stagnation streamline are plotted to see the effect of coupled radiation on the case. P1 and fvDOM models are used here. since N_2 is not a radiating gas hence, not much difference can be seen between with and without radiation. The peak temperature predicted by P1 and fvDOM model is slightly less than the no radiation one as heat transfer by radiation causes radiative cooling in the shock-layer region. A difference in the prediction of peak temperature of about 1.47 % for P1 and 2.037 % for fvDOM with no radiation case is observed.
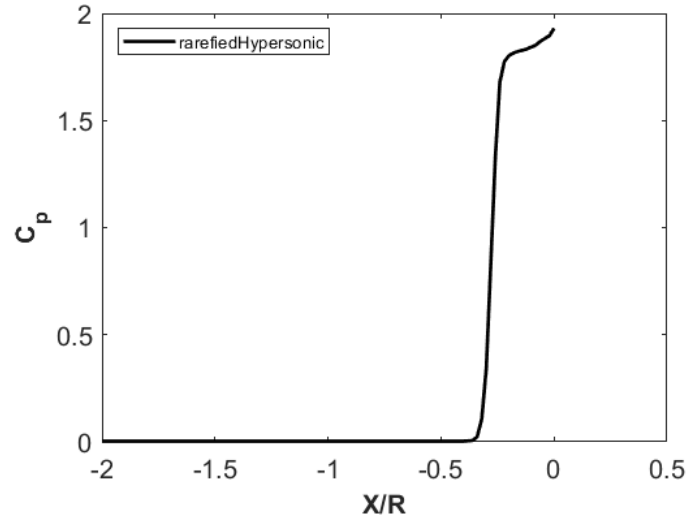
Figure 4.3: Distribution of C_p along the stagnation streamline

The shock stand-off distance for all the three cases remains almost the same. Some disagreement of fvDOM with P1 and no radiation is seen in the boundary layer region. This is because of the gray gas assumption considered in this case as a constant value of absorption and emission coefficient is taken while it depends on pressure, temperature and wavelength for such hypersonic flow cases. C_p is also plotted in Figure 4.3. As soon as the flow hits the bow shock, the value of C_p rises sharply and then stays constant in the boundary layer region. The value for C_p is highest at the stagnation point.
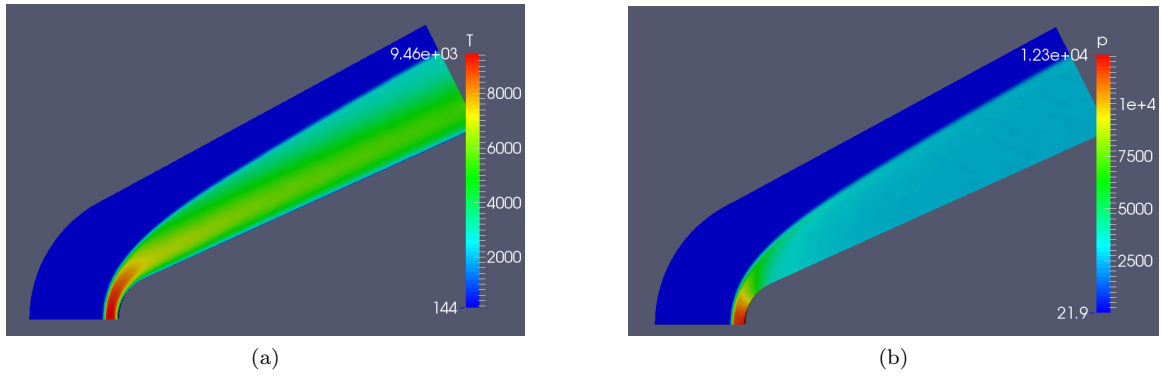

Figure 4.4: Contour of (a) temperature and (b) pressure for blunted cone case.
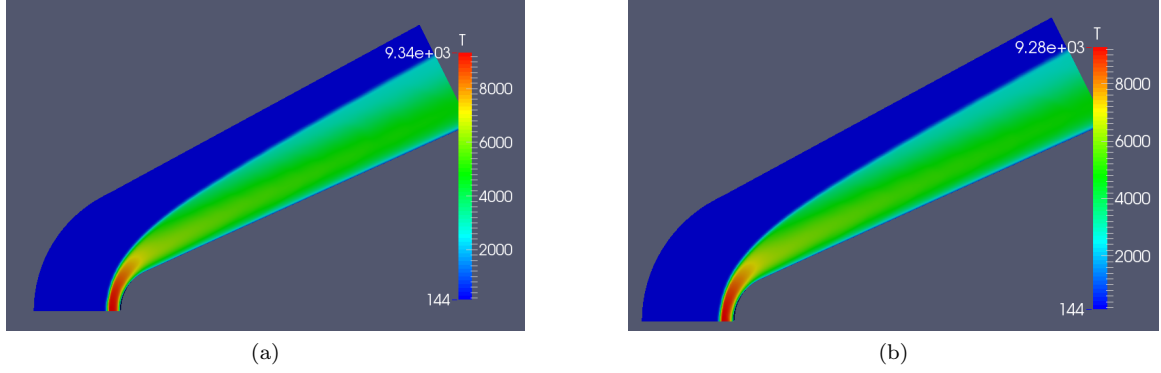
Figure 4.5: Contours of temperature for (a) P1 and (b) fvDOM radiation models.

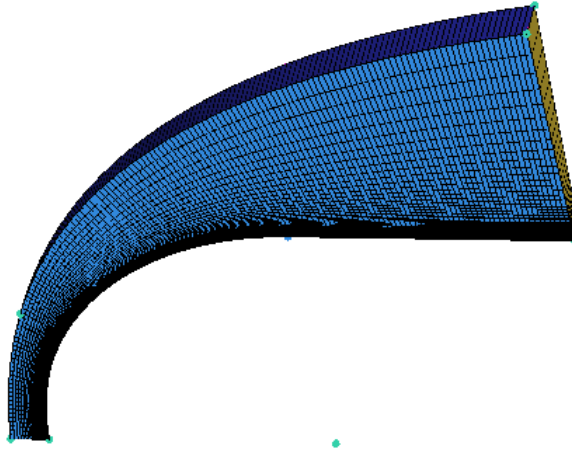## 4.2 Blunted Wedge Geometry

Figure 4.6: Mesh for high mach blunted wedge case

The interest of this study is to use the chemical models and high-temperature thermodynamic libraries to analyze the current case. In this case simulations have been performed on a blunted wedge geometry as discussed in section 3.2 but for a higher mach number and different degree of bluntness. Again dry air is considered as the test gas in this case. The flow conditions are given in Table 4.2 [27]. The simulations for this case is done at a higher mach no of 25.9. Hence, for this case ionization reactions cannot be ignored. An air chemistry model having 11 species ($N_2, O_2, NO, N, O, O^+, O_2^+, e^-, N^+, N_2^+, NO^+$) and 40 reactions (20 forward and 20 backward) is considered for this case [3]. Again a non-catalytic wall is assumed for all the species in this case. The species are assumed to be in thermodynamic equilibrium and state of the gas is governed by the single equilibrium temperature model.

Table 4.2: Flow simulation conditions for high mach blunted wedge case.

Test gas	Kn	$R(m)$	Type	Ma_∞	p_∞(Pa)	ρ_∞(kg/m^3)	T_∞(K)	T_w(K)
Dry air	0.006	0.1524	wedge	25.9	4.764	7.68e-05	216.0	1500

In Figure 4.7a, temperature is plotted along the stagnation streamline. The temperature increases adruptly and reaches its maximum value of around 16390 K. The massive amount of flow kinetic energy in a hypersonic freestream is converted to internal energy of the gas across the strong bow shock wave, hence creating very high temperatures in the shock-layer near the nose. In addition, downstream of the nose region, where the shock-layer has expanded and cooled around the body, we have a boundary layer with an outer-edge mach number that is still high, hence, the intense frictional dissipation within the hypersonic boundary layer creates high temperatures and causes to boundary layer to become chemically reactive. Due to this, the temperature is brought down to even lower values near the stagnation point because, the gas molecules have more time to dissociate since, the velocity decreases as the flow approaches the point. In Figure 4.7a, coefficient of pressure is also plotted along the stagnation streamline. The peak value for the same is observed to be 1.85. A shock stand-off distance of approximately 0.013 m is observed in this case.
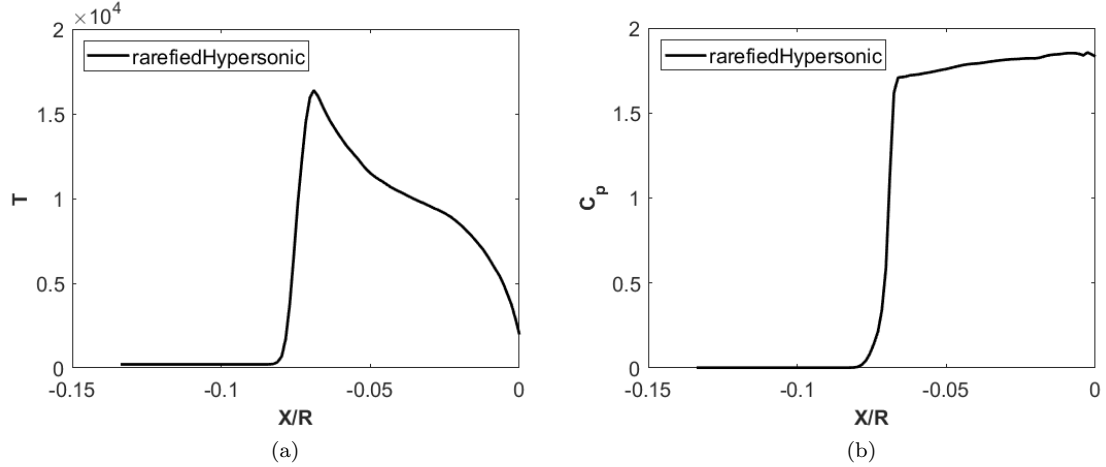
Figure 4.7: Distribution of (a) Temperature and (b) Coefficient of Pressure along the stagnation streamline for high mach blunted wedge case.
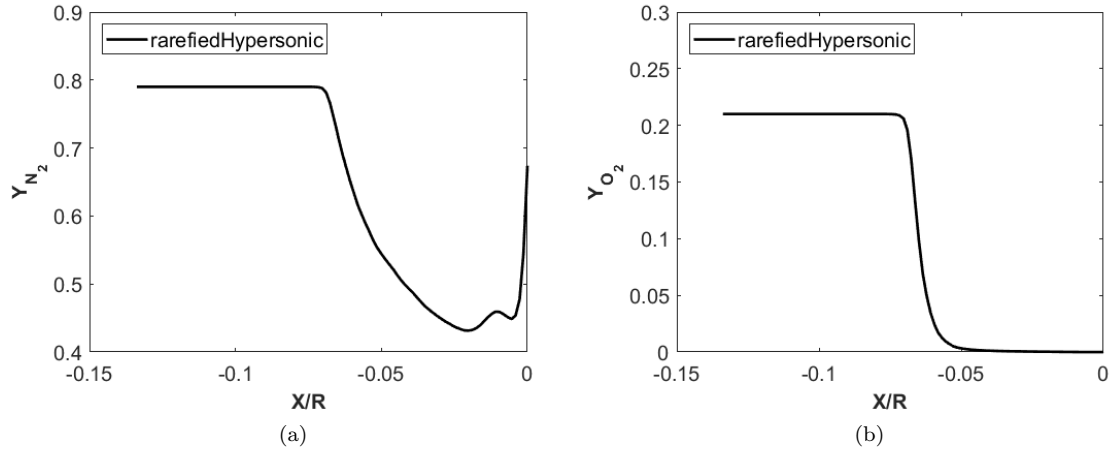

Figure 4.8: Distribution of mass fractions for (a) N_2 and (b) O_2 along the stagnation streamline for high mach blunted wedge case.

When ionization is present in the shock-layer, large number of electrons are provided throughout the layer. The free electrons can cause a communication blackout to and from the vehicle during parts of the entry trajectory as it absorbs the radio-frequency radiation. Hence, it is of high priority to determine the electron number density in the shock plasma region around the body. In Figure 4.8a and 4.8b the mass fractions for N_2 and O_2 are plotted. Since the boundary layer is chemically reactive, hence, dissociation and ionization reactions cause the concentration of N_2 and O_2 to decrease initially, then near the stagnation region recombination reaction takes place for $N2$ and its concentration again rises to 0.67. The ionization for both N_2 and O_2 starts above 9000 K. At such high temperatures partially ionised plasma is formed consisting of O, O^+, N, N^+ and $e^- s$. The main

25

increase in electron number density is mainly caused by NO^+ ions. The contours for temperature, pressure, electron density and mass fractions for N_2 and O_2 are presented below.

At such high velocities stgnation point radiative heat transfer is greater than or equal to the convective heat transfer. The absorption coefficient in this case should be a function of temperature, pressure, mass fraction and frequency but for simplicity a constant value is considered for this case [1]. In Figure 4.9, temperature profiles along the stagnation streamline are compared for no radiation and P1 model. The radiation energy lost from the flowfield results in a cooling effect that ultimately reduces temperature and shock thickness. Also the effect becomes greater as R is increased, refer Figure 3.4. There is a vast difference of about 2700 K between the peak values for with and without radiation. The shock thickness when compared to none radiation decreases by 26 % in this case.
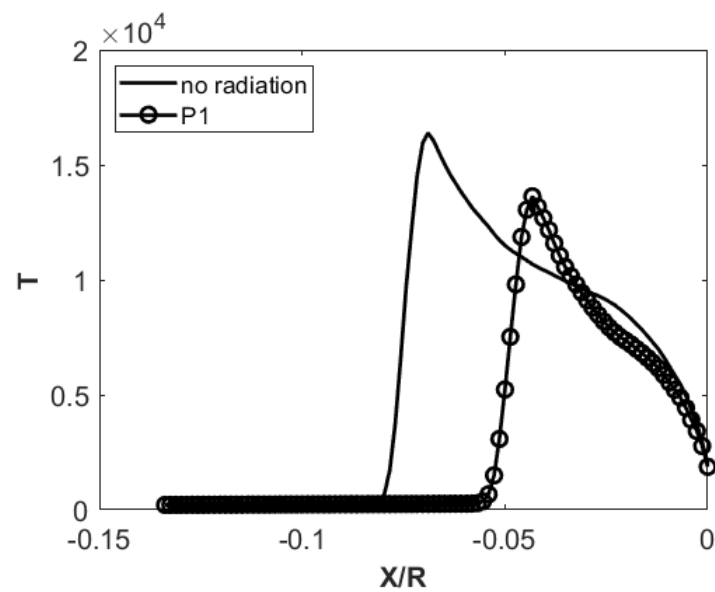
Figure 4.9: Comparison of temperature profile along the stagnation streamline for with and without radiation for high mach blunted wedge case.

(a)   (b)

Figure 4.10: Comparison of contours of temperature for (a) no radiation and (b) P1 model for high mach blunted wedge case.

Figure 4.11: Contour for electron distribution around high mach blunted wedge case

(a)   (b)
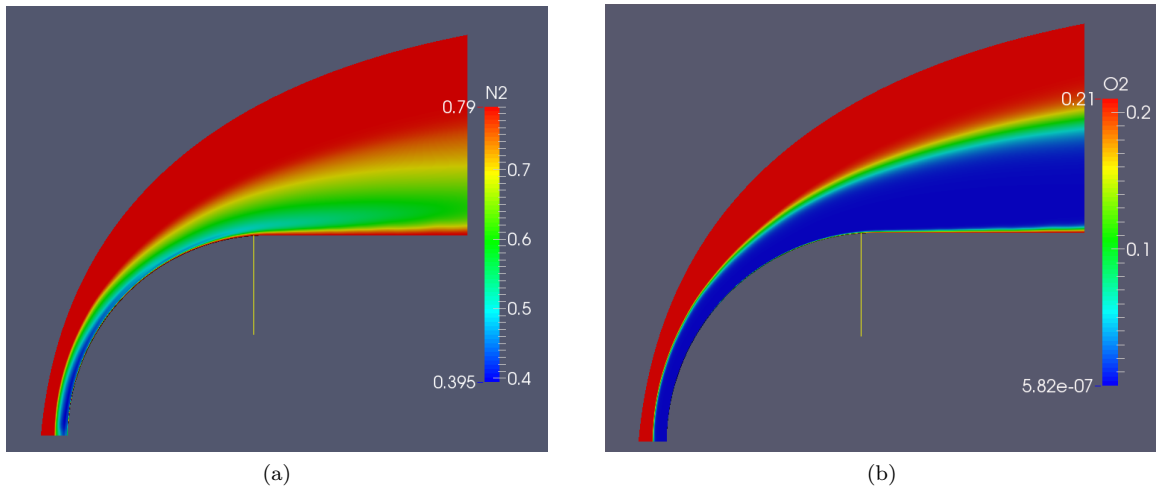
Figure 4.12: Contours of mass fractions of (a) $N2$ and (b) $O2$ for high mach blunted wedge case.

4.3   Crew Exploration Vehicle

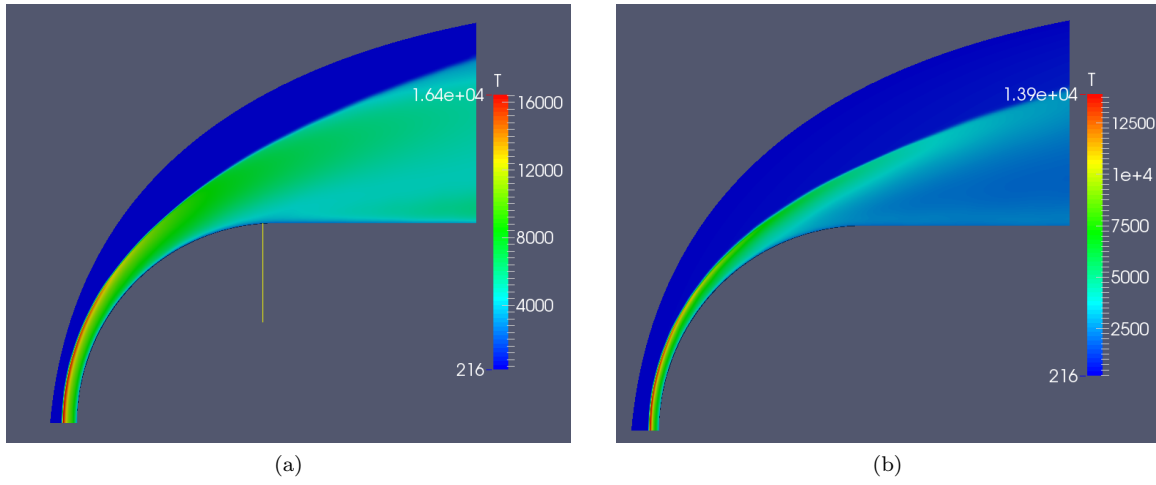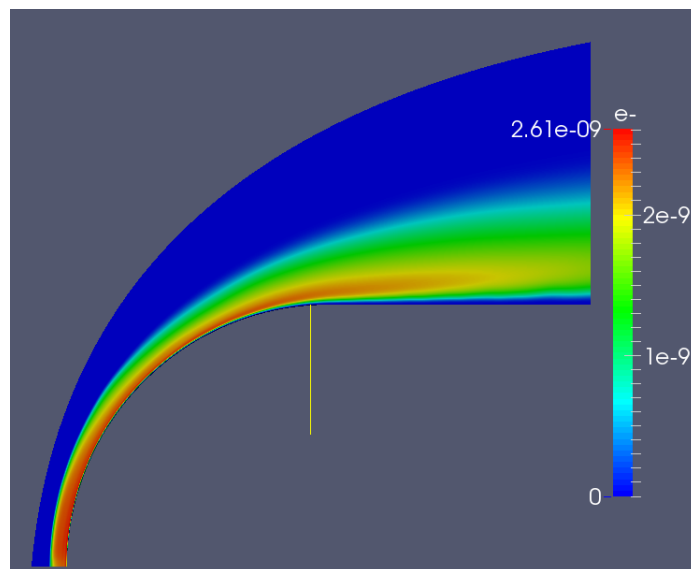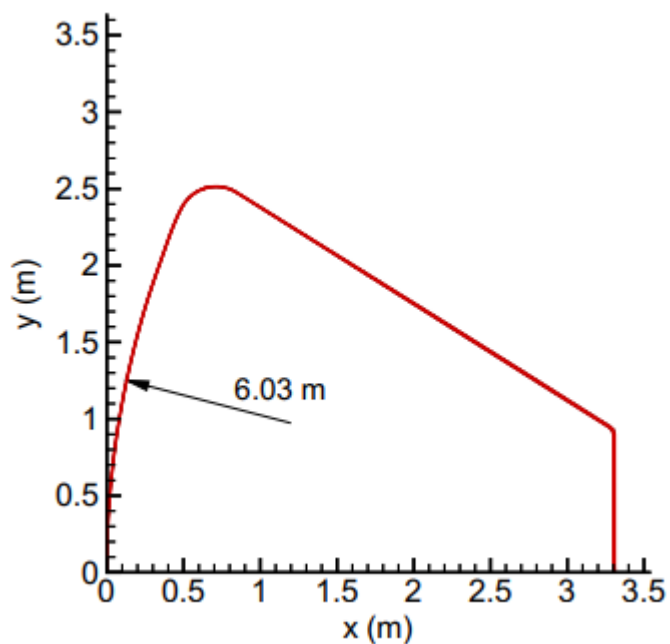Figure 4.13: Geometry for crew exploration vehicle (CEV)
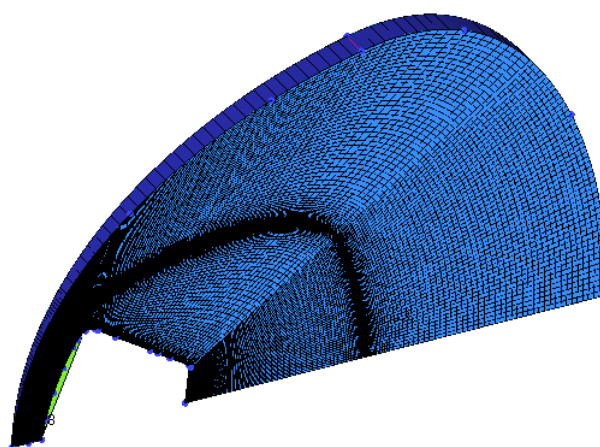
Figure 4.14: Grid generation for CEV

In this case simulations are performed on a reentry vehicle entering into Martian atmosphere. In Figure 4.13, the basic geometry of the vehicle is shown [11]. The spacecraft has a sphere-cone configuration with radius as 6m. Again in this case, the block is splitted and the mesh is made fine near the wall as well as across the shock wave for better results. The mesh is made in Ansys ICEMCFD and then is imported in OpenFOAM. To reduce the computation cost a 2D axisymmteric

mesh is used with a small wedge angle of 4 degrees. The boundary conditions are specified as hypersonic or freestream at the inlet, supersonic or zero gradient at the outlet, velocity slip and temperature jump conditions at the wall and the front and back planes are taken as symmetry. The intial mesh size along the normal direction (δy) is taken as 1.6 mm and along the vehicle (δx) as 1 mm. The total number of cells in the mesh are 120×150. Also, in this case a two equation Mentor Shear Stress Transport (MSST) is used as the turbulence model. The flow conditions for this case is described in Table 4.2. The Martian atmosphere has 98.07% of CO_2 by mass and 1.93% of N_2

Table 4.3: Flow simulation conditions for blunted cone case.

CO_2	N_2	Type	Ma_∞	u_∞(m/s)	p_∞(Pa)	ρ_∞(kg/m^3)	T_∞(K)	T_{wall}(K)
98.07%	1.93%	wedge	26.34	5000	10	3.7396e-04	140	300

CO_2 is the primary gas in Martian atmosphere. A mixture of several species is formed such as O, C, CO, CO_2 and O_2 when CO_2 starts dissociates while passing across the shock-layer region. The chemical kinetics include exchange reactions between atoms and molecules alongwith disscociation of CO, O_2 and CO_2. In this case since the temperature remains below 6000 K, hence ionization reactions are neglected. The presence of N_2 even in small amounts can significantly effect the flow-field, hence a more accurate chemistry model comprising of 9 species and 11 reactions is considered in this case as the martian composition is taken as 98.07% of CO_2 and 1.93% of N_2 by mass [6]. The arrhenius rate parameters for the same are described below in Table 4.3

Table 4.4: Arrhenius forward reaction rates for chemical reactions of Martian atmosphere.

Forward Reaction	$A(\frac{cm^3}{mols})$	β	$E_{ae}(cal/mol)$
$CO_2 + M \rightarrow CO + O + M$	6.9×10^{21}	-1.50	125600.8
$CO + M \rightarrow C + O + M$	2.3×10^{20}	-1.00	256065.0
$O_2 + M \rightarrow O + O + M$	2.0×10^{21}	-1.50	118603.7
$CO + O \rightarrow O_2 + C$	3.9×10^{13}	-0.18	137362.0
$CO_2 + O \rightarrow O_2 + CO$	2.1×10^{13}	0.00	55183.0
$N_2 + M \rightarrow N + N + M$	7.0×10^{21}	-1.60	224702.0
$NO + M \rightarrow N + O + M$	1.1×10^{17}	0.00	149867.0
$N_2 + O \rightarrow NO + N + M$	6.4×10^{17}	-1.00	76164.45
$CN + O \rightarrow NO + C$	1.6×10^{13}	0.10	28981.0
$CO + N \rightarrow CN + O$	1.0×10^{14}	0.00	76621.0
$N_2 + C \rightarrow CN + N$	1.1×10^{14}	-0.11	46052.0

In Figure 4.15a and 4.15b the temperature profile and coefficient of pressure are plotted along the stagnation streamline. The maximum temperature reached is around 5251 K and the maximum C_p value reached is 1.89. A shock stand-off distance of 0.283m is observed in this case. CO and O are the major species in the shock layer. Most of the CO_2 in this case is dissociated and some other species include undissociated CO_2 and some fraction of O_2. For some initial time of 1ms the

solution is evolved slowly with the CFL no kept as 0.01. The value of CFL no is increased to 0.3 after a developed solution is seen in the front portion of the vehicle. The final solution is presented for 0.01s.

In Figure 4.16a and 4.16b the mass fractions of CO and O are plotted. In the shock layer region the mass fraction of CO first increases sharply and then gradually to its peak value of 0.59. Similar nature of curve is observed for O with a lesser peak value of 0.2. The high temperature in the shock-layer region increases the vibrational energy of CO_2 causing it to dissociate into CO and O. In such cases radiative heat transfer can play a major role because CO_2 and CO have high values of absorption and emission coefficient. To compute the absorption and emission coefficients in this case, gray mean absorption-emission polynomial as a function of temperature given by Centeno et al. is used [29]. In Figure 4.17 comparison of temperature profiles are done for with and without radiation. Not much difference is seen as the temperature is not high enough for the radiative heat trasnfer to be dominant. A difference of about 278 K exists between the peak temperatures and a shock deviation of about 10.7 % is seen. Since $CO_2 and CO$ are radiating gases, hence, at higher mach numbers and bluntness significant dissimilarities can be seen between no radiation and coupled radiation.
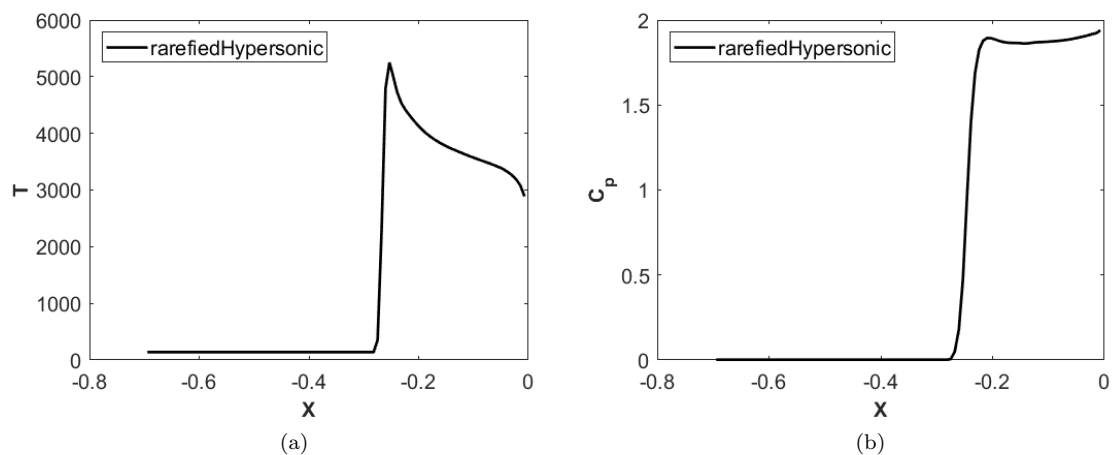

Figure 4.15: Distribution of (a) Temperature and (b) Coefficient of Pressure along the stagnation streamline for CEV case.

Contours of temperature, pressure, velocity and mass fractions of CO and O are presented seen below. The recirculation zone formed because of the sharp edge of the vehicle geometry can be clearly seen in the velocity contour (Figure 4.18a) and temperature contour (Figure 4.18b).A recirculation length of 4.7m is observed in this case.

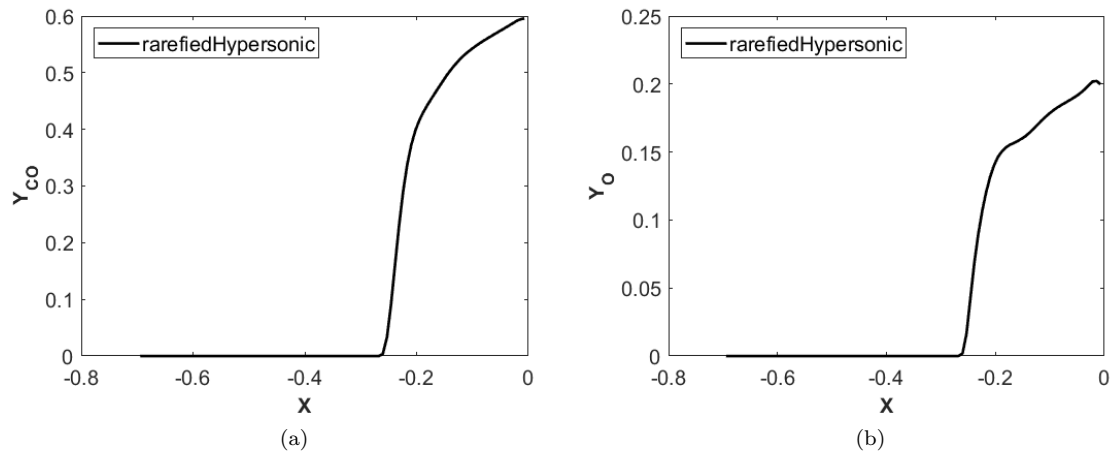Figure 4.16: Distribution of mass fractions for (a) CO and (b) O along the stagnation streamline for CEV case.
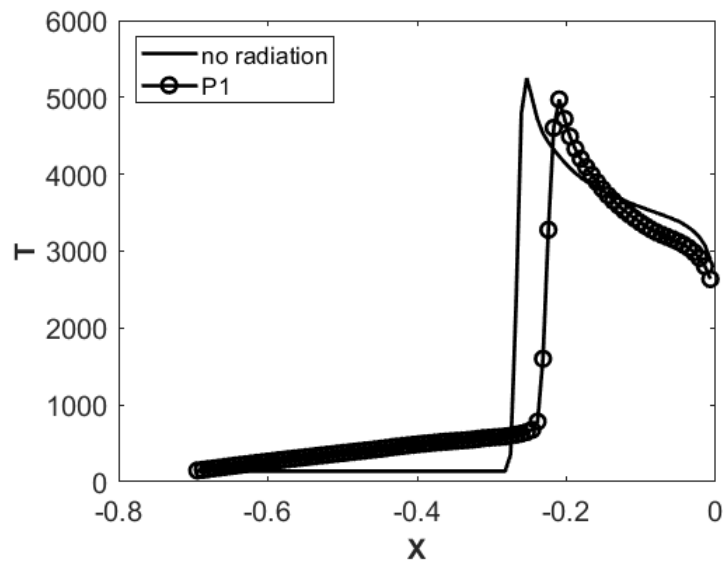

Figure 4.17: Comparison of temperature profile along the stagnation streamline for with and without radiation for CEV case.
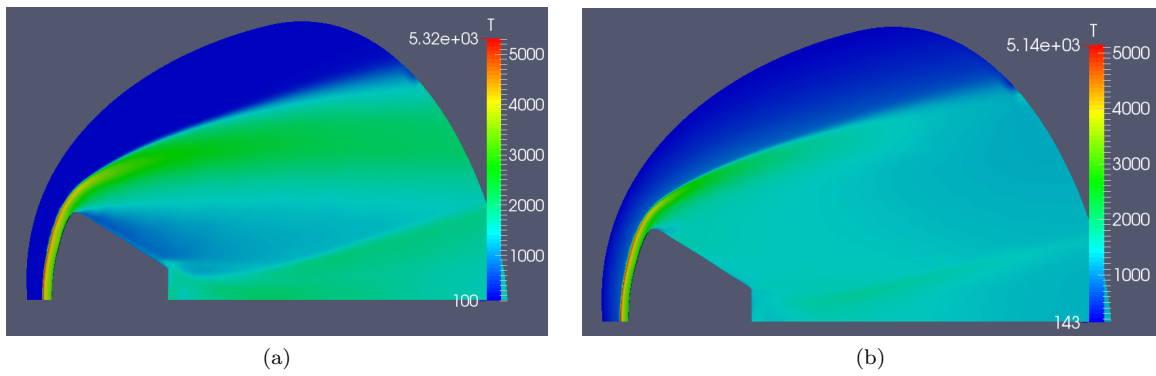
Figure 4.18: Comparison of contours of temperature for (a) no radiation and (b) P1 model for CEV case.
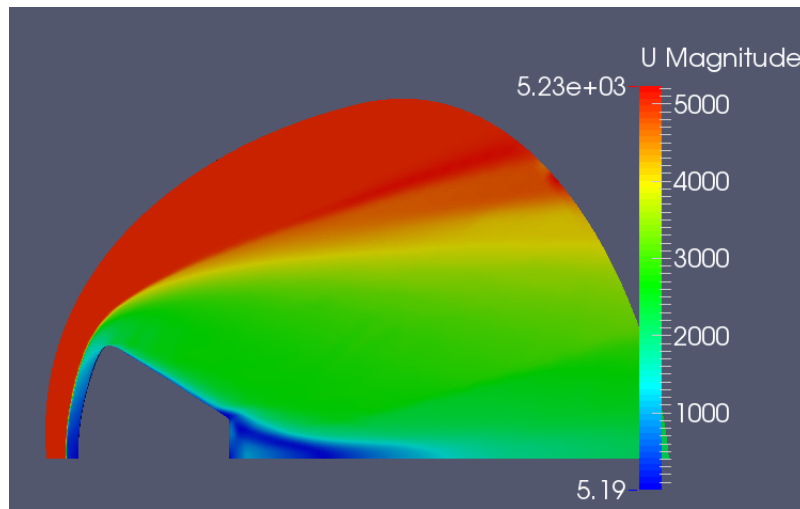

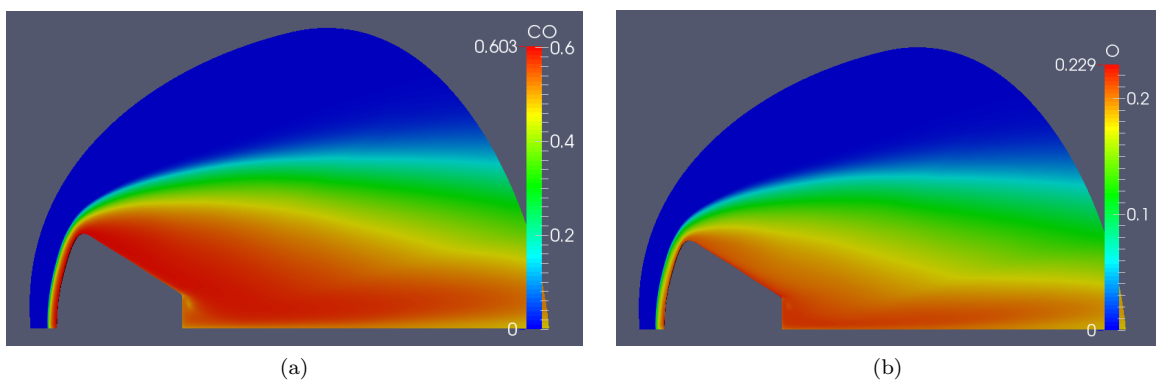Figure 4.19: Contour of magnitude of velocity for CEV case.

Figure 4.20: Contours of mass fractions of (a) CO and (b) O for CEV case.

Chapter 5

Conclusion

To compute the hypersonic flow with all non-equilibrium effects including radiative heat transfer, a new solver is created within OpenFOAM's framework [12]. Maxwells's velocity slip [20] and Smoluchowski temperature jump [21] boundary conditions are used available in rhoCentralFoam solver. The capabilities of a density based solver for the computation of supersonic flow is used and merged with the pressure based solver which can handle chemical non-equilibrium within the flow (reactingFoam) to create $rarefiedHypersonicFoam$. The old thermodynamic libraries are updated within $rarefiedHypersonicFoam$. With the new libraries [15], the solver is now able to solve for high speed and temperature gas dynamics problem. The solver is coupled with radiation and pre-existing models available in OpenFOAM are used to study its effect over hypersonic flows.

The first objective of the work is to validate the solver for different cases and flow conditions on the basis of distribution of temperature, coefficient of pressure and species profiles along the stagnation streamline. The validations are done for two different cases. The first one involves single species(Ar), non-reacting flow at Mach 10 over a blunted flat plate case [26]. The simulation is done in slip flow regime. The solver is first validated against DSMC data for temperature and coefficient of pressure. Then after the validation, the case is run for with and without radiation. P1 and fvDOM models avaialble in OpenFOAM are used to solve for radiation. The temperature profiles for three different cases involving no radiation, P1 and fvDOM are compared. Significant reduction in peak temperature and shock stand-off distance is seen because of radiative cooling. fvDOM method, though being computationally expensive predicts better for optically thin medium compared to P1. The second case is done for a reacting flow in Earth's atmosphere at Mach 18 over a blunted wedge geometry [27]. A 5 species and 12 reactions air chemistry model is employed in this case [3]. The

temperature and species profile are compared with the work of Tchuen and Zeitoun. The current solver based on single temperature model predicts approximately the same peak temperature and shock stand-off distance when compared with the solver based on translational as well as vibrational temperature.

Once the solver is validated, the second objective is accomplished by using the solver to do the analysis on a wide variety of test cases. The solver is used to study three distinct cases. For the first case again single species(N_2), non-reacting flow conditions are chosen at Mach 20 over a blunted cone model [28]. The nature of profiles for temperature and coefficient of pressure are studied. Effect of radiation using P1 and fvDOM models are also studied. Not much deviation is seen in terms of temperature and shock distance as N_2 is a non-radiating gas and its optical thickness value is very low. For the next case, the same blunted wedge geometry with a larger nose radius is simulated [27]. The same air chemistry model used earlier is extended and ionization reactions are also considered in this case, hence 11 species and 40 reactions are used in this case [3]. The temperature, pressure and species are plotted along the stagnation streamline at Mach 25.9. The increase in electron number density and its formation around the body because of ionization reactions inside the boundary layer is witnessed with the help of contour. In this case, a more realistic study on Crew Exploration Vehicle cruising at a speed of 5 km/s through Martian atmosphere is done [11]. The mesh generation is done for a wedge case to save computational cost. Since, in the Martian atmosphere CO_2 acts as the primary gas hence, a totally different chemistry model is needed for the same. A 9 species and 11 reactions model is employed in this case [6]. The dissociation of $CO2$ within the boundary layer is seen using the mass fraction profiles for CO and O. Formation of recirculation region is also observed in this case.

In the future, a more realistic temperature, pressure and mass-fraction dependent mean absorption-emission model along with a scattering model will be used. The effect of solar radiation for high altitude cases will also be incorporated within the same solver.

Bibliography

[1] J. D. Anderson, *Hypersonic and High-Temperature Gas Dynamics*, 2nd ed. AIAA, 2006.

[2] M. F. Modest, *Radiative Heat Transfer*, 3rd ed. Academic Press, 2013.

[3] R. N. Gupta, J. M. Yos, R. A. Thompson, and K. P. Lee, "A Review of Reaction Rates and Thermodynamic and Transport Properties for an 11- Species Air Model for Chemical and Thermal Nonequilibrium Calculations to 30,000 K," *NASA RP-1232.*, 1990.

[4] C. Park, "Assessment of Two Temperature Kinetic Model for Ionizing Air," *Journal of Thermophysics and Heat Transfer.*, vol. 3, pp. 233 – 244, 1989.

[5] ——, "Review of Chemical-Kinetic Problems of Future NASA Mission, I: Earth Entries," *Journal of Thermophysics and Heat Transfer.*, vol. 7, pp. 385 – 398, 1993.

[6] C. Park, J. Howe, R. Jaffe, and G. V. Candler, "Review of Chemical-Kinetic Problems of Future NASA Missions, II: Mars Entries," *Journal of Thermophysics and Heat Transfer.*, vol. 8, pp. 9 – 23, 1994.

[7] Y. Liu, D. Prabhu, K. A. Trumble, D. Saunders, and P. Jenniskens, "Radiation modeling for the reentry of the Stardust sample return capsule," *Journal of Spacecraft and Rockets.*, vol. 47, pp. 741 – 752, 2010.

[8] D. Bose, E. McCorkle, C. Thompson, D. Bogdanoff, D. Prabhu, G. Allen, and J. Grinstead, "Analysis and model validation of shock layer radiation in the air," in *46th AIAA Aerospace Sciences Meeting and Exhibit*, 2008, p. 1246.

[9] A. Feldick, M. F. Modest, D. Levin, P. Gnoffo, and C. Johnston, "Examination of coupled continuum fluid dynamics and radiation in hypersonic simulations," in *7th AIAA Aerospace Sciences Meeting including The New Horizons Forum and Aerospace Exposition*, 2009, p. 475.

[10] M. J. Wright, D. Bose, and J. Olejniczak, "Impact of flowfield-radiation coupling on aeroheating for titan aerocapture," *Journal of Thermophysics and Heat Transfer.*, vol. 19, pp. 17 – 27, 2005.

[11] A. Bansal, A. Feldick, and M. F. Modest, "Simulation of hypersonic flow and radiation over a mars reentry vehicle using openfoam," in *50th AIAA Aerospace Sciences Meeting including the New Horizons Forum and Aerospace Exposition*, 2012, p. 650.

[12] OpenCFD, "OpenFOAM," http://www.openfoam.org/, 2010.

[13] A. Kurganov, S. Noelle, and G. Petrova, "Semidiscrete central-upwind schemes for hyperbolic conservation laws and HamiltonJacobi equations," *SIAM Journal on Scientific Computing.*, vol. 23, pp. 707 – 740, 2001.

[14] C. J. Greenshields, H. G. Weller, L. Gasparini, and J. M. Reese, "Implementation of semidiscrete, nonstaggered central schemes in a collocated, polyhedral, finite volume framework, for highspeed viscous flows," *International journal for numerical methods in fluids.*, vol. 63, pp. 01 – 21, 2010.

[15] B. J. McBride and S. Gordon, "CComputer Program for Calculation of Complex Chemical Equilibrium Compositions and Applications: Users Manual and Program Description," *NASA Reference Publication, No 1311*, 1996.

[16] H. Gijare, A. Bhagat, and N. Dongari, "Numerical investigation of a chemically reacting and rarefied hypersonic flow field," *Shock Waves.*, 2019.

[17] H. Gijare, A. Assam, and N. Dongari, "Aero-thermodynamics optimization of re-entry capsule in the slip flow regime," in *1st International ISHMT-ASTFE Heat and Mass Transfer Conference*, 2015, p. 487.

[18] R. B. Bird, *Transport Phenomena.* Applied Mechanics Reviews, 2002.

[19] W. G. Vincenti and C. H. Kruger, *Introduction to Physical Gas Dynamics.* Wiley New York, 1965.

[20] J. Maxwell, "Stresses in rarefied gases arising from inequalities of temperature," *Proceedings of the Royal Society of London.*, vol. 27, pp. 304 – 308, 1878.

[21] M. V. Smoluchowski, "ber wrmeleitung in verdnnten gases," *Annalen der Physik und Chemie.*, vol. 64, pp. 101 – 130, 1898.

[22] C. Park, "Calculation of radiation from argon shock layers," *Journal of Quantitative Spectroscopy and Radiative Transfer.*, vol. 11, pp. 29 – 40, 1982.

[23] M. Bartlova, N. Bogatyreva, and V. Aubrecht, "Radiation heat transfer in thermal argon plasma with iron vapors," *Plasma Physics and Technology.*, vol. 1, pp. 08 – 10, 2014.

[24] L. I. Kiselevskii and V. D. Shimanovich, "Optical properties of heated air, carbon dioxide, and argon," *Journal of applied spectroscopy.*, vol. 64, pp. 837 – 846, 1997.

[25] B. G. Lougou, Y. Shuai, X. Chen, Y. Yuan, H. Tan, and H. Xing, "Analysis of radiation heat transfer and temperature distributions of the solar thermochemical reactor for syngas production," *Frontier in Energy.*, vol. 11, pp. 480 – 492, 2017.

[26] H. S. Massimi, H. Shen, C. Y. Wen, Y. S. Chen, and S. M. Liang, "Numerical analysis of hypersonic flows around blunt- nosed models and a space vehicle," *Aerospace Science and Technology.*, vol. 43, pp. 360 – 371, 2015.

[27] G. Tchuen and D. E. Zeitoun, "Effect of chemistry in nonequilibrium hypersonic flow around blunt nosed models," *Journal of thermophysics and heat transfer.*, vol. 23, pp. 433 – 442, 2009.

[28] V. Casseau, "An Open-Source CFD Solver for Planetary Entry," Ph.D. dissertation, University of Strathclyde, Scotland, 2017.

[29] F. R. Centeno, R. Brittes, F. H. R. Franca, and O. A. Ezekoye, "Evaluation of gas radiation heat transfer in a 2D axisymmetric geometry using the line-by-line integration and WSGG models," *Journal of quantitiative spectroscopy and radiative transfer.*, vol. 156, pp. 1 – 11, 2015.